Controlling protein adsorption on graphene for cryo-EM using low-energy hydrogen plasmas

Christopher J Russo & Lori A Passmore

Despite its many favorable properties as a sample support for biological electron microscopy, graphene is not widely used because its hydrophobicity precludes reliable protein deposition. We describe a method to modify graphene with a low-energy hydrogen plasma, which reduces hydrophobicity without degrading the graphene lattice. Use of plasma-treated graphene enables better control of protein distribution in ice for electron cryo-microscopy and improves image quality by reducing radiation-induced sample motion.

Improved electron microscopes, more-stable cryo-stages and direct electron detectors with high quantum efficiency have recently brought about a revolution in biological electron microscopy (EM), enabling determination of three-dimensional (3D) structure at near-atomic resolution for several molecular complexes[1,2]. Even so, specimen preparation methods have remained largely unchanged since they were initially developed for electron cryo-microscopy (cryo-EM) almost three decades ago[3].

Thin films of amorphous carbon (am-C) are typically used as EM supports (grids). Am-C films are often semiconducting, and their conductivity and mechanical strength (with a Young's modulus of 0.2–200 GPa) can be reduced by several orders of magnitude, depending on the conditions during their production[4]. This makes am-C and the ice that it supports prone to surface charging and radiation-induced chemical and physical changes[5] that lead to blurring of particle images and degradation of information content[2,6,7]. Because conditions are not well controlled during the fabrication of most am-C support membranes, there is a large variation in their performance; microscope time and samples are often wasted on poor substrates. In contrast, graphene[8], an atomically thin, mechanically robust conductor, comprises a near-ideal substrate for imaging nanoscale specimens by EM. Suspended graphene conducts charge ballistically over the submicron distances that span a hole used for imaging molecules in ice[8]; this should reduce the buildup of surface charge during electron-beam exposure. Further, graphene's in-plane mechanical strength (Young's modulus of 1 TPa)[9] is the highest ever measured for any material.

Despite graphene's potential advantages, the ease of its large-scale manufacture by chemical vapor deposition (CVD) and some promising preliminary work on its use as a substrate for biological molecules[10–13], graphene has not been widely adopted for use with biological specimens. There are two reasons for this: graphene is hydrophobic, thus precluding the deposition of proteins from aqueous solutions, and it is susceptible to surface contamination during manufacturing, handling and storage. Previous attempts to use graphene as an EM support required either harsh solvents that are incompatible with most proteins or conversion of the graphene to graphene oxide[11,12]. Graphene oxide is less than ideal because (i) it contributes nearly as much background signal as does thin am-C (ref. 11), (ii) it is often an insulator and therefore is less able to neutralize accumulated surface charge[14] and (iii) it has decreased mechanical strength, which makes it less stable than graphene.

Recently, investigators have shown that it is possible to convert graphene to its fully hydrogenated form, graphane, by extended hydrogen-plasma treatments[15]. Here we demonstrate that ≤5% hydrogenation of graphene with a low-energy hydrogen plasma can address the two problems described above by removing surface contamination and making graphene suitably hydrophilic for use with proteins.

A low-energy, pure hydrogen plasma contains H, H^+, H_2^+, H_3^+ and free electrons[16]. We hypothesized that the primary chemical reaction of graphene with hydrogen plasma is hydrogenation via the reaction: sp^2 C + H $\rightleftharpoons$ sp^3 CH. We assessed the change in hydrophobicity of a graphene surface in response to a hydrogen plasma by measuring the static contact angle between water, air and graphene (**Fig. 1a**). With increasing plasma dose, the contact angle decreased exponentially from a value of 91 ± 0.5° to a saturation value of 66 ± 1.3° (s.e.). This corresponds to a reduction in the graphene-water interfacial energy of 0.19 ± 0.02 eV/nm^2 (**Supplementary Note 1**). To monitor the conversion to graphane, we measured the change in the lattice constant[15] after plasma exposure, by using electron diffraction (**Fig. 1b–d** and **Supplementary Fig. 1**). After an 80-s dose of plasma treatment, less than 20% of the carbon-carbon sp^2 bonds were converted to carbon-hydrogen sp^3. Furthermore, the sharp peaks in the diffractograms after plasma treatment (**Fig. 1c**,**d**) demonstrated that the underlying graphene lattice was preserved.

We studied graphene's properties as a substrate for cryo-EM before and after plasma treatment as compared to those of am-C. When suspended graphene is prepared by typical transfer methods, it is usually contaminated with adsorbents (**Fig. 1e**). Exposing the graphene to 30 s of hydrogen-plasma treatment removed most

Medical Research Council Laboratory of Molecular Biology, Cambridge, UK. Correspondence should be addressed to L.A.P. (passmore@mrc-lmb.cam.ac.uk).

RECEIVED 20 MARCH 2013; ACCEPTED 28 FEBRUARY 2014; PUBLISHED ONLINE 20 APRIL 2014; DOI:10.1038/NMETH.2931

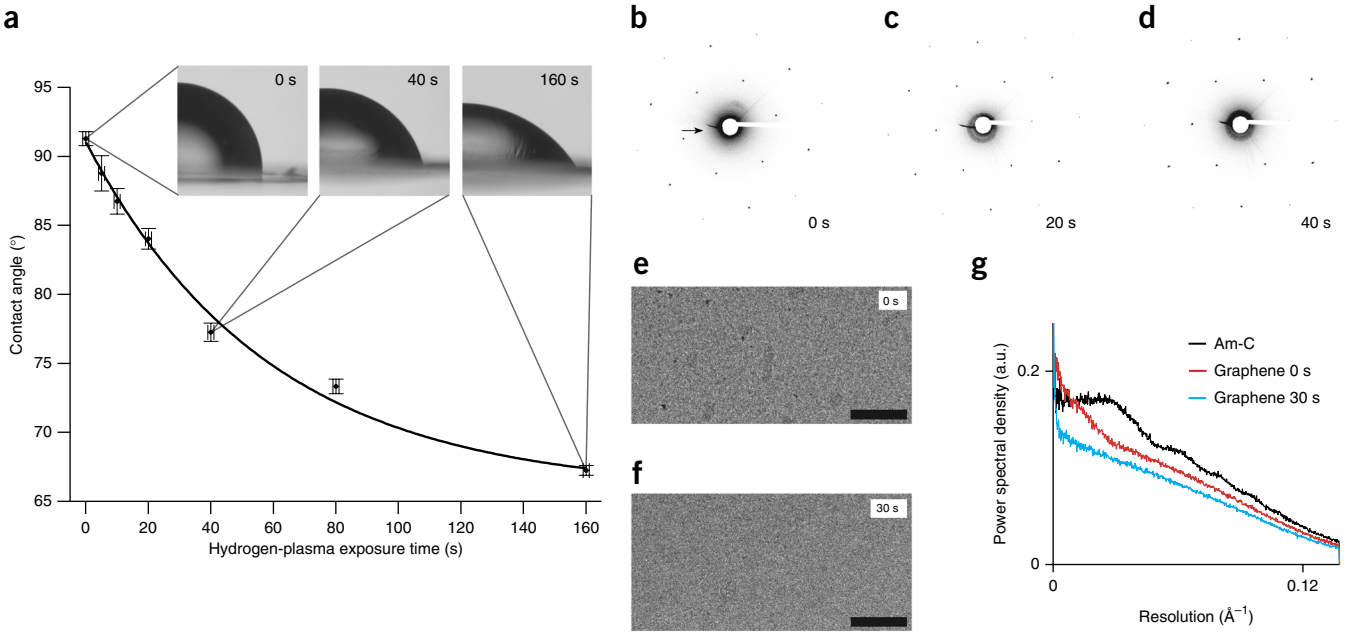

Figure 1 | Low-energy hydrogen-plasma treatment renders graphene hydrophilic and removes contamination. (**a**) Plots of the air-water-graphene contact angle versus exposure time, with insets containing examples of optical micrographs used to measure the angles. The curve is an exponential fit to the data, with a rate constant of 1/58 s^{-1}. Error bars, s.e. at each plasma dose for the 3–5 measurements in *y* (exact *n* values in Online Methods) and the estimated accuracy of the exposure time, ± 1 s, in *x*. (**b**–**d**) Selected area electron-diffraction patterns for the same suspended graphene sample before hydrogen-plasma exposure (**b**) after 20 s (**c**) and after 40 s (**d**) of exposure. Arrow points to the 0–110 reflection at 2.14 Å and sets the scale for all three diffractograms. The change in the lattice constant for **c** and **d** relative to **b** is less than the error in the measurement and is ≈0.9% (**Supplementary Fig. 1**). (**e**,**f**) Electron micrographs of suspended graphene before (**e**) and after (**f**) 30-s hydrogen-plasma treatment, respectively. Scale bars, 1,000 Å; nominal defocus, –2.0 µm; fluence (electron dose), 25 e^{-}/Å^2. (**g**) Power spectral density in each complete micrograph (**Supplementary Fig. 2**), normalized to the total image intensity, for am-C with 28 ± 1.4 Å thickness (**Supplementary Fig. 2e**), graphene before plasma treatment (as in **e**) and graphene after plasma treatment (as in **f**). A.u., arbitrary units.

of the surface contamination (**Fig. 1f**) and decreased the background signal level in the image (**Fig. 1g**). Compared to that of a thin layer (28 ± 1.4 Å) of am-C (**Supplementary Fig. 2**), the background signal of the treated graphene lattice was much lower and was featureless (**Fig. 1g**).

Hydrogen-plasma treatment probably removes surface contamination much faster than it modifies graphene, because hydrocarbon contaminants are easily broken down and volatilized by the energetic plasma. Because the graphene sp^2 bond is highly resistant to chemical modification, it is reduced only slowly by hydrogen in the plasma. Hydrogen species in the 10-eV to 15-eV range used here have insufficient energy to directly remove carbon atoms from their sp^2 bonds (21 eV), thus eliminating sputtering damage to the lattice[17].

Having shown that we could control the hydrophobicity of graphene, we then tested hydrogen plasma–treated graphene as a substrate for cryo-EM by using purified ribosomes. We transferred monolayer graphene to holey carbon EM grids, subjected the grids to various doses of hydrogen plasma and used them to prepare vitrified ice samples containing 70S ribosomes. On grids without graphene, very few ribosomes were visible in the ice (~60 particles/µm^2), because most were attracted to the surface of the am-C and to the edges of the holes (**Fig. 2a** and **Supplementary Fig. 3**). When we used the same concentration, freezing and blotting conditions with graphene grids treated with hydrogen plasma for 10 s, only small patches of vitreous ice and clumped ribosomes were visible (**Fig. 2a**). This indicated incomplete wetting and was consistent with the small change in contact angle at this dose. After a 20-s treatment with hydrogen plasma the graphene surface was more uniformly wet, and the ice quality was greatly improved, thus demonstrating that ribosomes adsorbed to the surface (~600 particles/µm^2). Increasing the plasma dose to 40 s led to very densely packed ribosomes (~1,900 particles/µm^2). Selected area diffractograms acquired after each image confirmed the vitreous nature of the ice and verified the presence of the graphene layer (**Supplementary Fig. 4**). Overall, our results demonstrate a monotonic relationship between hydrogen-plasma dose and surface particle density, thereby allowing the use of graphene to tune particle distribution.

To demonstrate that adsorption to partially hydrogenated graphene is not specific to the 70S ribosome, we also tested the 80S ribosome (**Supplementary Fig. 5**), the 20S proteasome (**Fig. 2b** and **Supplementary Fig. 6a**) and apoferritin (**Fig. 2c** and **Supplementary Fig. 6b**). 80S ribosomes have a ten-fold-higher density on graphene grids compared to grids without an additional support. The density of proteasome particles on the graphene surface was sixfold higher than that in the unsupported ice and was probably near saturation, owing to steric effects. Apoferritin showed a >500-fold increase in particle surface density on graphene.

To study cryo-EM image quality on graphene, we determined the 3D structure of the 70S ribosome from three micrographs on graphene (**Supplementary Fig. 5**). Using 2,061 individual particle images, we obtained a reconstructed density map at 19-Å resolution (**Supplementary Fig. 7**). Next we calculated a reconstruction from 20,050 80S particles on graphene (**Supplementary Fig. 5**), to a resolution of 5.0 Å (**Supplementary Fig. 7**). Using these data, we

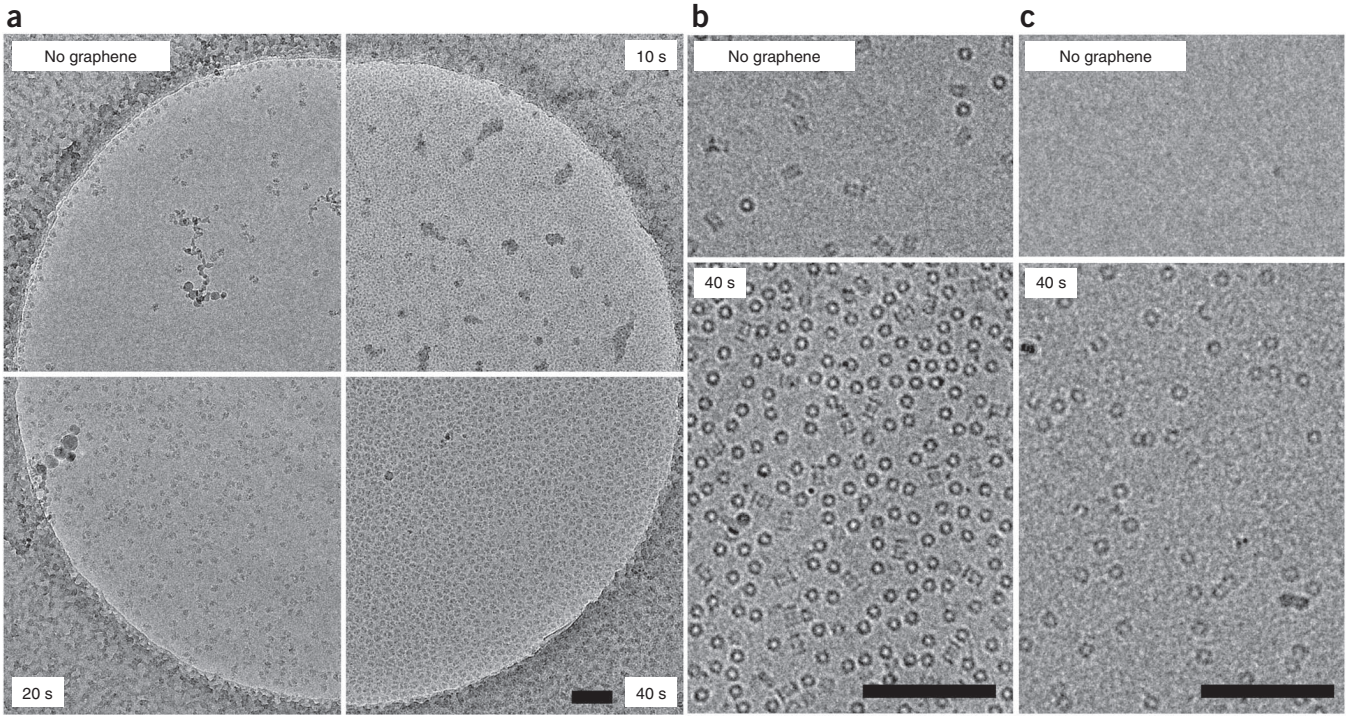

Figure 2 | Dose-dependent adsorption of proteins on hydrogen plasma–treated graphene. (**a**) Cryo-EM micrographs of 70S ribosomes in vitrified ice at 80 K. Upper left quadrant is a standard grid treated with a 10-s hydrogen-plasma dose. The other three quadrants show grids covered with monolayer graphene and treated with 10, 20 or 40 s of hydrogen plasma as indicated. All other sample concentration, blotting, vitrification and imaging conditions are the same for all four grids. Scale bar, 1,000 Å. Full micrographs are shown in **Supplementary Figure 3**. (**b**,**c**) Electron micrographs of 20S proteasome (**b**) or apoferritin (**c**) molecules on graphene treated with 40 s of hydrogen plasma (bottom) and molecules in unsupported ice from an adjacent region of the same grid (top). Scale bars, 1,000 Å. Magnification is the same for **b** and **c**. Full micrographs for **b** and **c** are shown in **Supplementary Figure 6**.

assessed the quality of the images on graphene. Imperfections in particle images are often characterized with an empirical model of short-range atomic motion (*B* factor), which provides a measure of the image quality. We observed an ~35% reduction in the *B* factor of 80S ribosomes on graphene compared to am-C, a result indicative of the improvement in the information content of each particle image.

To investigate the origins of the improved image quality, we analyzed movie data of individual particles acquired with a direct electron detector for 80S ribosomes on three substrates: am-C, unsupported ice and graphene (**Fig. 3**). We used the individual frames of the movies to determine the trajectory of each particle and then calculated the r.m.s. ensemble displacement for each frame for thousands of particles on each test grid and repeated the measurements for multiple grids (**Fig. 3** and **Supplementary Fig. 8**). We found that 80S-ribosome particles in ice irradiated with high-energy electrons exhibited two distinct phases of motion: an initial fast phase from 0 to ~6 $e^-/Å^2$ and a subsequent slower phase. Relative to conventional grids, the speeds of the first and second phases were reduced 10–20% and 30–50%, respectively, on graphene; this probably accounts for the improved image quality on graphene. We note the striking differences in radiation-induced movement from grid to grid for conventional grids. Although some conventional grids performed similarly to graphene grids

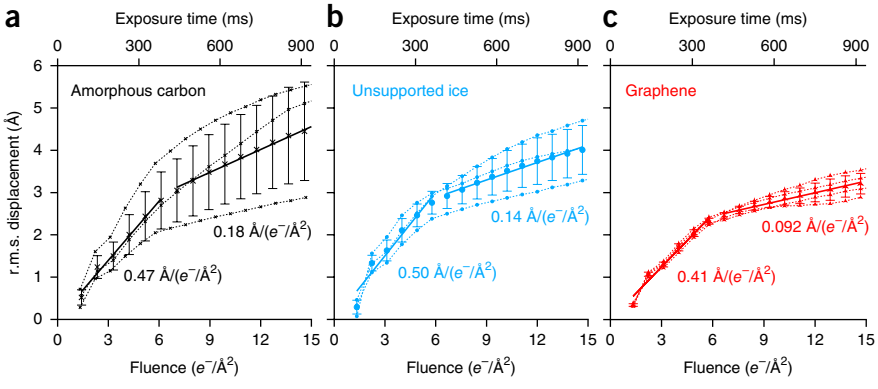

Figure 3 | Reduced motion of proteins on graphene substrates, as shown by speed plots. The average 80S-ribosome displacement from its initial position is plotted versus time and electron fluence for data collected in ice, with support by a continuous layer of am-C (**a**), without any support layer (**b**) or with support by a graphene substrate (**c**). Each point (along dotted lines) represents the r.m.s. displacement of thousands of particles from a single grid (numbers of particles in Online Methods), whose positions were measured with a five-frame running average under constant electron-beam irradiation (300 keV; 16 $e^-/Å^2/s$. Solid lines are the linear fits to the two phases of motion, with the slopes (ensemble particle speed) as indicated. Error bars, s.e.m. of the replicate experiments (three separate grids for **a** and **b**; four for **c**). All plots have the same scale.

(**Fig. 3** and **Supplementary Fig. 8**), there was a much larger variation from one conventional grid to the next, probably owing to uncontrolled differences in conductivity and mechanical properties. The well-defined and reproducible mechanical and electrical properties of graphene are likely to account for its more consistent performance.

In summary, we have demonstrated that a low-energy hydrogen plasma can nondestructively modify graphene hydrophobicity. Surprisingly, even the addition of one hydrogen atom for every 20 carbon atoms renders graphene hydrophilic and induces protein adsorption. We propose a simple model (**Supplementary Note 2**) to understand this large change in interfacial energy (~7 kT/nm^2) and its saturation with only partial hydrogenation of the lattice[18].

A major problem with conventional cryo-EM grids is the lack of precise control of the distribution of proteins within a thin layer of vitreous ice. During blotting and vitrification, proteins often segregate to the air-water interface or to other surfaces present. The use of hydrogen plasma–treated graphene enables better control of particle surface density, independently of other sample-preparation variables (concentration, humidity, blot time, etc.). Additionally, the specific adsorptive properties of the hydrogen-treated graphene surface allow the use of much lower concentrations of protein, for example, 150 times less for the case of apoferritin and ten times less for 80S ribosomes.

Another problem in cryo-EM is specimen-dependent degradation of image quality[7]; this can be improved in two ways with hydrogen plasma–treated graphene. First, graphene is effectively invisible at resolutions used in structural biology (>2.1 Å), thus leading to reduced background noise in the images compared to that in am-C. Second, graphene generally reduces electron radiation–induced particle movement (image blurring) and thus increases the information in each image. We speculate that such movement is caused by a complicated buildup of charge and stress on the specimen[19,20], including the creation of large electric fields across regions of the irradiated area, electrical breakdown of the ice layer in response to these fields, density changes within the ice due to radiolysis, and mechanical release of stresses in the ice created during vitrification. Further work is needed to elucidate the detailed dynamics and underlying mechanisms of these particle motions.

Hydrogen plasma–treated graphene offers a reproducible and tunable surface for the adsorption of proteins. We predict that the preparation of biological specimens for cryo-EM will move from a trial-and-error art to a systematic screening of surface conditions through a range of plasma treatments. We also expect that low-energy plasma treatment of graphene-based sensors will enable the detection and characterization of specific biological molecules and complexes.

METHODS

Methods and any associated references are available in the online version of the paper.

Note: Any Supplementary Information and Source Data files are available in the online version of the paper.

ACKNOWLEDGMENTS

We thank J.A. Golovchenko for the use of a chemical vapor–deposition instrument at Harvard for graphene synthesis during the initial phases of this work; S. Scotcher for fabrication of custom sample holders and copper punch machines; I.S. Fernandez, A. Kelley and V. Ramakrishnan of the Medical Research Council (MRC) Laboratory of Molecular Biology for the gift of ribosomes; J. Grimmett, T. Darling, G. McMullan and S. Chen for technical assistance; and E. Rajendra, R.A. Crowther, D. Neuhaus, X.C. Bai, S. Scheres, N. Unwin, A.R. Faruqi and R. Henderson for helpful discussions and comments. This work was supported by the European Research Council (ERC) under the European Union's Seventh Framework Programme (FP7/2007-2013)/ERC grant agreement no. 261151 to L.A.P., an MRC (UK) Centenary award to C.J.R. and MRC (UK) grant MC_U105192715 (L.A.P.).

AUTHOR CONTRIBUTIONS

C.J.R. designed and performed the experiments and analyzed the data. C.J.R. and L.A.P. designed experiments, planned the project, interpreted the results and wrote the manuscript.

COMPETING FINANCIAL INTERESTS

The authors declare competing financial interests: details are available in the online version of the paper.

1. Grigorieff, N. & Harrison, S.C. *Curr. Opin. Struct. Biol.* **21**, 265–273 (2011).
2. Bai, X.-C., Fernandez, I.S., McMullan, G. & Scheres, S.H. *Elife* **2**, e00461 (2013).
3. Dubochet, J. *et al. Q. Rev. Biophys.* **21**, 129–228 (1988).
4. Robertson, J. *Adv. Phys.* **35**, 317–374 (1986).
5. Miyazawa, A. *et al. J. Mol. Biol.* **288**, 765–786 (1999).
6. Brilot, A.F. *et al. J. Struct. Biol.* **177**, 630–637 (2012).
7. Henderson, R. & McMullan, G. *Microscopy* **62**, 43–50 (2013).
8. Geim, A.K. *Science* **324**, 1530–1534 (2009).
9. Lee, C., Wei, X., Kysar, J.W. & Hone, J. *Science* **321**, 385–388 (2008).
10. Russo, C.J. A structural imaging study of single DNA molecules on carbon nanotubes. PhD thesis, Harvard Univ. (2010).
11. Pantelic, R.S., Meyer, J.C., Kaiser, U., Baumeister, W. & Plitzko, J.M. *J. Struct. Biol.* **170**, 152–156 (2010).
12. Pantelic, R.S. *et al. J. Struct. Biol.* **174**, 234–238 (2011).
13. Sader, K. *et al. J. Struct. Biol.* **183**, 531–536 (2013).
14. Gómez-Navarro, C. *et al. Nano Lett.* **7**, 3499–3503 (2007).
15. Elias, D.C. *et al. Science* **323**, 610–613 (2009).
16. Méndez, I. *et al. J. Phys. Chem. A* **110**, 6060–6066 (2006).
17. Russo, C.J. & Golovchenko, J.A. *Proc. Natl. Acad. Sci. USA* **109**, 5953–5957 (2012).
18. Israelachvili, J. & Pashley, R. *Nature* **300**, 341–342 (1982).
19. Curtis, G.H. & Ferrier, R.P. *J. Phys. D Appl. Phys.* **2**, 1035–1040 (1969).
20. Downing, K.H., McCartney, M.R. & Glaeser, R.M. *Microsc. Microanal.* **10**, 783–789 (2004).

ONLINE METHODS

Graphene synthesis. Graphene was synthesized by CVD on copper-foil substrates[21,22]. Briefly, an ~18 cm^2 section of 25-μm copper foil (Alfa Aesar 13382) was placed in the 25-mm-diameter quartz tube of a dry-pumped CVD furnace, evacuated to <20 mTorr and then exposed to a continuous flow of hydrogen (99.999%) gas at a flow of 20 SCCM, thus bringing the pressure in the reaction tube to 500 mTorr. The temperature of the oven was elevated under thermocouple control to 1,000 °C over the course of ~15 min. Once the temperature was reached, an additional 20 SCCM of methane (99.999%) was added to the reaction chamber for a duration of 15 min, thus bringing the total pressure to 700 mTorr. After methane addition was complete, the heating was turned off, and the reaction tube was slowly cooled to ambient temperature under continuing hydrogen flow over a period of 2 h. Once cool, the hydrogen flow was stopped, the chamber was vented with dry nitrogen, and the graphene on copper foil was removed from the growth tube and stored in a critically cleaned Fluorware wafer container inside a clean low-humidity storage box until use.

Hydrogen-plasma treatment and contact-angle measurement. To measure the graphene-water contact angle, individual 3.2-mm-diameter disks were punched from the graphene on copper foils with a custom-made disk punch. Disks were initially cleaned by submersion for 10 s in CMOS-grade isopropyl alcohol (Sigma). After the residual solvent evaporated, they were placed on a nitric acid–cleaned glass slide inside a commercial plasma reaction chamber (Fischione 1070) where the grids were located 15 ± 1 cm from the edge of the RF coils. The design of this instrument is such that the acceleration of ions across the plasma sheath is minimized, so high-energy species are not expected to contribute to reactions at the graphene surface[23]. The source of hydrogen was an electrolysis high-purity hydrogen generator (Dominik Hunter 20H-MD). Controls for the zero-time exposure dose included those with and without various solvent-cleaning treatments; we found that the contact angle was the same for all to within experimental error. Each disk was mounted in an optical microscope (Zeiss Axiophot), a 1-μL droplet of 18 MΩ (5.5×10^{-8} S/cm) deionized water was applied, and disks were immediately (within 5 s upon withdrawal of the pipette tip) imaged with a calibrated digital camera attached to the microscope (Zeiss ERc5s). We measured the droplet evaporation rate (1.4 nL/s) and found that it contributed a negligible change in angle (<0.5°) during the delay between water application and image acquisition. Each image was subsequently analyzed to obtain the contact angle by graphical measurement of the angle between the substrate plane and the tangent to the droplet at the point at which it met the surface. This measurement was performed 3–5 times for each of the plasma doses (n = 5, 3, 5, 5, 4, 5, 4); the values were then normalized by division by the ratio of the droplet volume measured in the image to the value for the zero-plasma dose. We found that this normalization was required to correct for the error in pipetting a volume this small. The multiple measurements were then averaged and the standard error of the mean taken as the error in angle at each dose. Finally, we confirmed the presence of graphene covering the punched disks by subsequently transferring the graphene to EM grids, as described below, and then imaging them with an electron microscope. We note that the contact angle of 91° for intrinsic graphene (**Fig. 1a**) is well within the wide range of reported values[24]. Contact angles in the 60–80° range are typically used for protein deposition on standard am-C substrates[25]. The rate constant of the exponential fit was 1/58 s^{-1}.

Graphene-grid preparation. To create suspended-monolayer graphene EM grids, we use a method based on one first described by Regan *et al.*[26] and further developed in ref. 10. We started by cleaning commercial holey carbon on 300-mesh gold grids (Quantifoil Au 300 1.2/1.3) by using anticapillary tweezers to immerse them individually in chloroform, acetone and isopropyl alcohol for ~15 s each (Sigma-Aldrich, ultra-high-purity semiconductor-grade solvents). We found that this helped to remove any residual photoresist and large surface contaminants remaining on the Quantifoil films after manufacture. After blotting the grids dry in air, we then mounted them in a custom-made stainless-steel suspension holder inside the plasma reactor mentioned above. The chamber was evacuated to $<10^{-5}$ Torr, and then ultra-high-purity argon and oxygen (BOC 99.9999%) were admitted in a mass ratio of 9:1 to a steady-state pressure of 21 mTorr. The autotuned RF plasma was sparked at 40 W (<3 W reverse power) and applied for the specified time, in this case 10–30 s, for cleaning the grid. Quantifoil grids were then used immediately for graphene transfer.

To cover the Quantifoil grid with a graphene monolayer, a 3.2-mm disk of graphene on copper was cut from a larger foil with a custom-made mechanical punch. The disk was immersed in acetone and isopropanol (Sigma, CMOS grade) for 10–15 s each and blotted dry before use. The plasma-cleaned Quantifoil grid was then applied, carbon side down, to the disk. An optical microscope (Zeiss Axiophot) was used to inspect the grid 'sandwich' and make sure that both the grid and the disk were flat, free of particulate contaminants and in good contact with each other before the next step. Then 7 μL of CMOS-grade isopropyl alcohol was added to the top of the grid, and the droplet was allowed to dry in air. The receding meniscus of the alcohol pulled the carbon film of the Quantifoil into contact with the graphene surface, as verified by the change in the color of the reflected light from the surface.

Next, the grid-disk sandwich was floated in ~50 mL of buffered $FeCl_3$ (Sigma) in a crystallization dish for 20 min. The grid was then transferred with a flamed platinum loop to 32% HCl (Sigma CMOS grade) for 5 min and then to 10% HCl for 5 min. This was followed by three rinses in 18-MΩ deionized water. After the final water step, the grid was transferred with the loop to a piece of filter paper (Whatman no. 1) in an acid-washed glass petri dish and stored in a low-humidity box until use. All steps of the graphene transfer were monitored with an optical microscope. Grids were discarded if there were any defects.

Diffraction studies of hydrogen-treated suspended graphene. Selected area diffraction studies of suspended graphene were performed before and after hydrogen-plasma exposure in the following way. First, CVD-grown graphene was transferred to a precleaned Quantifoil grid as described above. The grid was mounted in a single-tilt holder (FEI) that had been cleaned with a 75%:25% Ar/O_2 plasma at 50 W for 5 min. The grid was imaged with 300 keV electrons in an FEI Tecnai F30 microscope whose residual column pressure was nominally 88 nTorr (measured

at the closest ion pump) and with an anticontamination shield surrounding the sample cooled by liquid nitrogen. Selected area diffractograms were collected on a liquid-cooled 2,048 × 2,048 CCD camera (Tietz F224HD) with a fluence of ~30 $e^-/Å^2/s$, a nominal camera length of 690 mm, exposure time of 1 s, and a 10-μm-diameter selected area aperture, which corresponded to an interrogated area of 0.30 $μm^2$ at the sample. The actual camera length was calibrated with the 111–311 lattice reflections of a thin film of polycrystalline aluminum. After the first diffractogram was collected, the sample was removed from the column and immediately transported in a sealed, carefully cleaned container while still mounted in the holder to the plasma chamber, exposed to pure hydrogen plasma (with the same conditions as above) while mounted in the holder, and then immediately returned to the electron microscope for collection of the second data set. During repeated experiments with this transfer process, we saw no evidence of contamination of the graphene sample. The systematic error in the measurement limits the precision to about 0.9% (**Supplementary Fig. 1**). Final diffractograms were inverted to black on white to improve contrast when printed.

Vitrification and electron cryo-microscopy with hydrogen plasma–treated graphene grids. Frozen stocks of *Thermus thermophilus* 70S[27] or *Saccharomyces cerevisiae* 80S[2] ribosomes provided by the V. Ramakrishnan lab were thawed and diluted in 5 mM HEPES, pH 7.5, 50 mM KCl, 10 mM NH_4Cl, 10 mM Mg acetate, and 6 mM β-mercaptoethanol (70S) or in 3 mM HEPES-KOH, pH 7.45, 6.6 mM Tris acetate, pH 7.2, 3 mM NH_4Cl, 6.6 mM NH_4 acetate, 48 mM K acetate, 4 mM Mg acetate, and 2.4 mM DTT (80S), all while being kept on ice. Ribosomes were used at 70 nM (70S) or 80 nM (80S) for graphene- or carbon-supported grids and at 800 nM for unsupported Quantifoil grids. Horse spleen apoferritin (Sigma) and human 20S proteasomes (Enzo) were diluted to 100 nM in phosphate-buffered saline, pH 7.4. Grids were treated with a pure hydrogen plasma as described above, for the indicated times, just before use. For the data sets used for 3D ribosome reconstructions and radiation-induced motion measurements, the hydrogen-plasma exposure time was 20 s, just before use, and the dose for the apoferritin and proteasome was 40 s. 70S-ribosome grids were placed in a cryo-plunger (FEI Vitrobot IV) equilibrated to 4 °C and 100% relative humidity; 3 μL of sample was applied, allowed to incubate for 60 s, blotted with force setting −20 for 2 s, and then plunged into liquid ethane at just above its melting point. 80S-ribosome, proteasome and apoferritin grids were placed in a nearly identical cryo-plunger (FEI Vitrobot III) and prepared with empirically equivalent settings: the cryo-plunger was equilibrated to 4 °C and 100% relative humidity; 3 μL of sample was applied, allowed to incubate for 15 s, blotted with force setting −2 mm for 5 s, and then plunged into liquid ethane at just above its melting point. Grids were then stored in liquid nitrogen until they were transferred to an electron microscope for imaging. Previously published cryo-EM studies of apoferritin[28] required sample concentrations that were ~150 times greater (15 μM versus 100 nM used here), presumably because most molecules are lost to other surfaces present during the blotting process.

For the 80S data in **Supplementary Figure 5**, we made four individual grids with varying plasma doses. The first grid examined had a 15-s hydrogen-plasma treatment. It had a low density of particles but was otherwise good. The second grid examined had a 20-s hydrogen-plasma treatment. The particle density was excellent, and all our data were collected from this grid. The remaining grids were discarded without examination. For the data in **Figure 2a**, we prepared two Quantifoil grids and one graphene grid for each hydrogen-plasma condition. All grids had suitable ice, except for the one with 10-s hydrogen-plasma treatment, which was too hydrophobic to wet properly. For the additional data in **Figure 3**, we prepared four graphene grids, all of which had good ice, and chose three for data collection. Thus, the failure rate for preparing cryo-specimens on graphene substrates is very low.

Vitrified 70S ribosomes were imaged with 300 keV electrons in a Polara (FEI) under very low-dose conditions (2.5 $e^-/Å^2/s$; <0.2 $e^-/Å^2$ preexposure in low-mag mode) at a nominal magnification of 23,000× at a temperature of 80–90 K. Exposures were 1 s on a CMOS direct electron detector (FEI back-thinned Falcon II) for which the calibrated pixels corresponded to $(4.58\ Å)^2$ at the sample, and the frame rate was 17 frames per second.

Vitrified 80S ribosomes were imaged with 300 keV electrons in a Titan Krios (FEI) under low-dose conditions ($16 \pm 3\ e^-/Å^2/s$; <0.2 $e^-/Å^2$ preexposure in low-mag mode) at a nominal magnification of 59,000× (**Supplementary Fig. 5**) or 47,000× (additional data in **Supplementary Fig. 8**) at a temperature of 80–90 K. Exposures were 1 s on a CMOS direct electron detector (FEI back-thinned Falcon II) for which the frame rate was 18 frames per second, and calibrated pixels corresponded to $(1.34\ Å)^2$ or $(1.75\ Å)^2$ at the sample. The condenser lens and aperture settings were such that the electron beam was circularly symmetric about the center of the grid hole and encompassed an area about 10–15% larger than the area of the suspended ice. On the basis of the symmetry of the interacting region, this illumination geometry minimizes the possible development of local electric fields and empirically gave the best images. All high-resolution data herein were collected with this illumination geometry. The first and last frames of the collection were discarded, owing to incomplete blanking of the beam. The region of the grid used for data collection had >95% single-layer graphene coverage as verified by electron diffraction on about every fifth hole after image acquisition. A typical micrograph of 80S ribosomes on graphene is shown in **Supplementary Figure 9**.

Single-particle data analysis. For the 70S data set, 2,282 particles were picked from three micrographs with EMAN2's boxer program with the semiautomated swarm method[29]. Next, the particles were preprocessed and extracted in boxes of 76 × 76 pixels (scale is 4.58 Å/pixel) in Relion[30], which included CTF fitting with CTFFIND3 (ref. 31). After one round of two-dimensional (2D) classification with 18 classes, 221 particles were discarded, and the remaining 2,061 were used for 3D refinement. The 3D refinement was carried out in Relion with an initial model generated from the 70S crystal structure[32], low-pass filtered to 50 Å. The 3D refinement converged at an estimated angular accuracy of 3.6° and a resolution of 19.3 Å (0.143 gold-standard FSC). The final map was low-pass filtered to 19.3 Å. The angles assigned to each particle imaged in the final refinement iteration (rotation and tilt in Relion) were used to generate the plot of orientations (**Supplementary Fig. 5b**). A combined structure from PDB 2WDK and 2WDL[32] was fit to the map with UCSF Chimera's rigid body–fitting algorithm[33]. The 3D renderings of the maps and models were created in Chimera.

doi:10.1038/nmeth.2931

The 80S data set on graphene shown in **Supplementary Figure 5c,d** comprised 48,386 particles picked from 401 micrographs, again with EMAN2's boxer program with the semiautomated swarm method. Micrographs were gain-corrected after collection by division by the sum of all the images, normalized to the mean value. Particles were preprocessed and extracted in boxes of 328 × 328 pixels with Relion, including CTF fitting with CTFFIND3. 11 micrographs were rejected, owing to poor CTF fits. After three rounds of 2D classification, 20,050 particles were kept for refinement in three dimensions. The majority of particles removed at this stage were individual 60S subunits. We used 20,050 particles imaged on am-C with the same data-collection strategy (fluence, exposure time, voltage, etc.), randomly selected from a previously published data set[2], for comparison. To facilitate comparison, we used the same initial model with the same coordinate orientation (EMD-1780)[34], low-pass filtered to 60 Å. All other refinement parameters were the same for the two data sets. The 3D refinement used gold-standard FSC calculations to prevent overfitting of the high-resolution data, as implemented in Relion's 3D autorefine algorithm[35]. FSC curves were calculated between the two halves of the data with the automated masking procedure in Relion post process. Resolutions of the reconstructions cited in the text were determined with the gold-standard method with a 0.143 criterion[36]. *B*-factor changes noted in the text were calculated for linear fits to unsharpened, uncorrected Guinier plots between 10.0 Å and 5.2 Å for both data sets[36].

Sample preparation and data collection for the additional data sets (**Fig. 3**) collected in unsupported ice (standard Quantifoil grid, no continuous carbon-support layer), on am-C and on graphene were identical to the above. The numbers of particles used for comparison were 20,050 (graphene data from above), 8,676, 9,481 and 2,715 for graphene; 55,837, 15,014 and 8,807 for unsupported ice; and 20,050 (previously published, glow discharged[2]), 32,751 and 9,819 for am-C.

Orientation distribution analysis. We assessed the orientational distribution of the ribosomes on the graphene substrate and compared it to that of am-C with the same number of particles randomly chosen from a previously published data set on the same ribosome sample[2]. We plotted the result with a Mollweide equal-area projection (**Supplementary Fig. 5b,d**). Although proteins generally exhibit preferential orientations relative to any interacting surface, we found that the orientational distribution for 70S on hydrogen plasma–treated graphene was better (more optimal coverage of Fourier space) than on glow-discharged am-C, whereas for 80S, it was somewhat worse compared to the previously published result[2] (**Supplementary Fig. 5**). Interestingly, even though the preparation of the graphene surface and the resultant particle surface density are nearly the same for 70S and 80S samples, the orientational distribution is different. Although every surface, including an air-water interface, is expected to influence the orientational distribution of proteins in thin layers of water, it will be specific to each protein-surface interaction and may be influenced by solution conditions and the presence of other amphiphilic species such as detergents. Further work will be required to understand, control and improve the orientational distributions of molecules on different substrates.

Speed plots. To measure the motion of the particles on the various grids, we first determined their positions at each movie frame in the micrograph with cross-correlation as implemented in Relion. To improve positional accuracy, five-frame running averages were used for the calculation. At the two ends of the movie, the averages for the first and last frames and the second and penultimate frames were averaged over the adjacent three and four frames respectively. The coordinates assigned to each particle for each frame were used to calculate the r.m.s. particle displacements for the entire particle ensemble versus time/dose. For speed-plot calculations, an ensemble comprised a set of particles from an individual grid. Each grid ensemble is plotted separately in **Figure 3** and **Supplementary Figure 8**, where a dotted line connects each data point. We calculated the mean value for the various ensemble trajectories on a particular type of grid and plotted those (large markers) as well as the standard error of the mean (error bars). With these data points, we calculated linear fits with regression analysis including a weighting function to account for the errors. The results are tabulated in **Supplementary Table 1**.

Because the initial position of the particle before irradiation is unknown, we must make some assumption to set the zero of the displacement curve. Here we took the *y* intercept from the fit to the first phase of motion as the best available estimate of the initial position of the particle. This includes as much information as possible about where the particle was located at the initiation of irradiation, but it is only approximate because the equation of motion for the particles during electron irradiation is unknown. In addition, to set the zero-exposure time, we had to account for the speed of the blanking relative to the timing of frame acquisition. Because the detector is continuously acquiring frames, the first collected frame in the exposure is triggered by the unblanking of the beam, which occurs somewhat randomly but on average is in the middle of the frame. This frame is discarded, but we add time equivalent to half a frame in the ensemble calculations to set the absolute zero of exposure time and fluence shown in **Figure 3**. On the basis of the accuracy of the clocking of the detector frame-acquisition times, the accuracy of the beam current measurement and stability, and the beam blanking speeds, we estimate the error in the exposure time per frame and the variation in electron fluence per frame to be <1% for all frames, the error in the absolute electron flux to be 20–30%, and the relative variation in electron flux between the different experiments to be <5%.

Finally, we also used newly developed motion-correction algorithms[2] to correct for particle motion during 3D reconstruction. We found that this gave very little improvement of the reconstructed map for graphene data, whereas the same algorithms applied to the same sample with larger particle motions on am-C did result in improvement of the reconstruction (**Supplementary Fig. 7b**). This agrees with the fact that we have reduced the motion of the particles, so motion correction is less effective.

Atomic force microscopy. To accurately measure the thickness of carbon films, a portion of the carbon layer as evaporated on mica was cleaved off with adhesive tape (3M Scotch Crystal) to leave behind a step edge. This was imaged in constant force, DC mode with an oxide-sharpened, contact-mode silicon tip/cantilever (Mikromasch CSC37) in air at ambient conditions in an atomic

force microscope (MFP3D, Asylum Research). After a 2D topographic image was obtained, the height was flattened with a 2D, second-order-polynomial fit to the masked mica surface and rendered with a grayscale as indicated in the images (**Supplementary Fig. 2d**). A histogram of the height values was created, and the two peaks representing the substrate and carbon surfaces were fit with Gaussian functions (**Supplementary Fig. 2e**). The parameters of these fits were then used to measure the height and calculate the error in the measurement (standard deviation).

21. Reina, A. *et al. Nano Lett.* **9**, 30–35 (2009).
22. Li, X. *et al. Science* **324**, 1312–1314 (2009).
23. Lieberman, M.A. & Lichtenberg, A.J. *Principles of Plasma Discharges and Materials Processing* 2nd edn. (Wiley, 2005).
24. Taherian, F., Marcon, V., van der Vegt, N.F.A. & Leroy, F. *Langmuir* **29**, 1457–1465 (2013).
25. Dubochet, J., Groom, M. & Mueller-Neuteboom, S. *Adv. Opt. Electron Microsc.* **8**, 107–135 (1982).
26. Regan, W. *et al. Appl. Phys. Lett.* **96**, 113102 (2010).
27. Selmer, M. *et al. Science* **313**, 1935–1942 (2006).
28. Wasilewski, S., Karelina, D., Berriman, J.A. & Rosenthal, P.B. *J. Struct. Biol.* **180**, 243–248 (2012).
29. Tang, G. *et al. J. Struct. Biol.* **157**, 38–46 (2007).
30. Scheres, S.H.W. *J. Struct. Biol.* **180**, 519–530 (2012).
31. Mindell, J.A. & Grigorieff, N. *J. Struct. Biol.* **142**, 334–347 (2003).
32. Voorhees, R.M., Weixlbaumer, A., Loakes, D., Kelley, A.C. & Ramakrishnan, V. *Nat. Struct. Mol. Biol.* **16**, 528–533 (2009).
33. Pettersen, E.F. *et al. J. Comput. Chem.* **25**, 1605–1612 (2004).
34. Armache, J.-P. *et al. Proc. Natl. Acad. Sci. USA* **107**, 19754–19759 (2010).
35. Scheres, S.H.W. & Chen, S. *Nat. Methods* **9**, 853–854 (2012).
36. Rosenthal, P.B. & Henderson, R. *J. Mol. Biol.* **333**, 721–745 (2003).

doi:10.1038/nmeth.2931

Controlling protein adsorption on graphene for cryo-EM using low-energy hydrogen plasmas

Christopher J. Russo[1] and Lori A. Passmore[1]

[1]Medical Research Council Laboratory of Molecular Biology, Cambridge CB2 0QH, UK

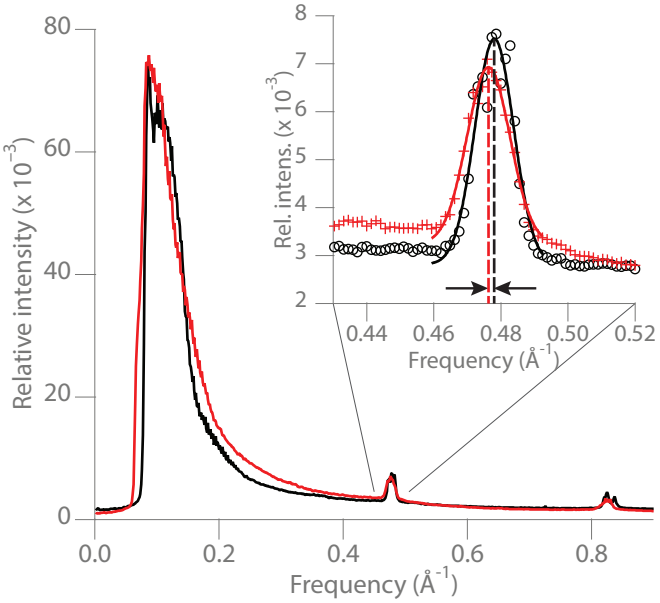

Supplementary Figure 1 | Azimuthal integral intensity plots from selected area diffractograms. Plots are azimuthally integrated diffractograms taken before and after 80 s hydrogen plasma treatment used to measure change in lattice constant vis a vis conversion to graphane. The difference in 0–110 peak position, shown with arrows, is –1.7 x 10^{-3} Å^{-1} which corresponds to a shift of –0.4 % in lattice constant. This is less than the precision of the measurement from sample to sample, which is limited by the variation in lattice constant (≅0.9%) due to stretching of the graphene layer on the grid. Previous studies of graphane formation showed that the lattice constant decreases by ≅5% upon full conversion to graphane[15].

Nature Methods: doi:10.1038/nmeth.2931

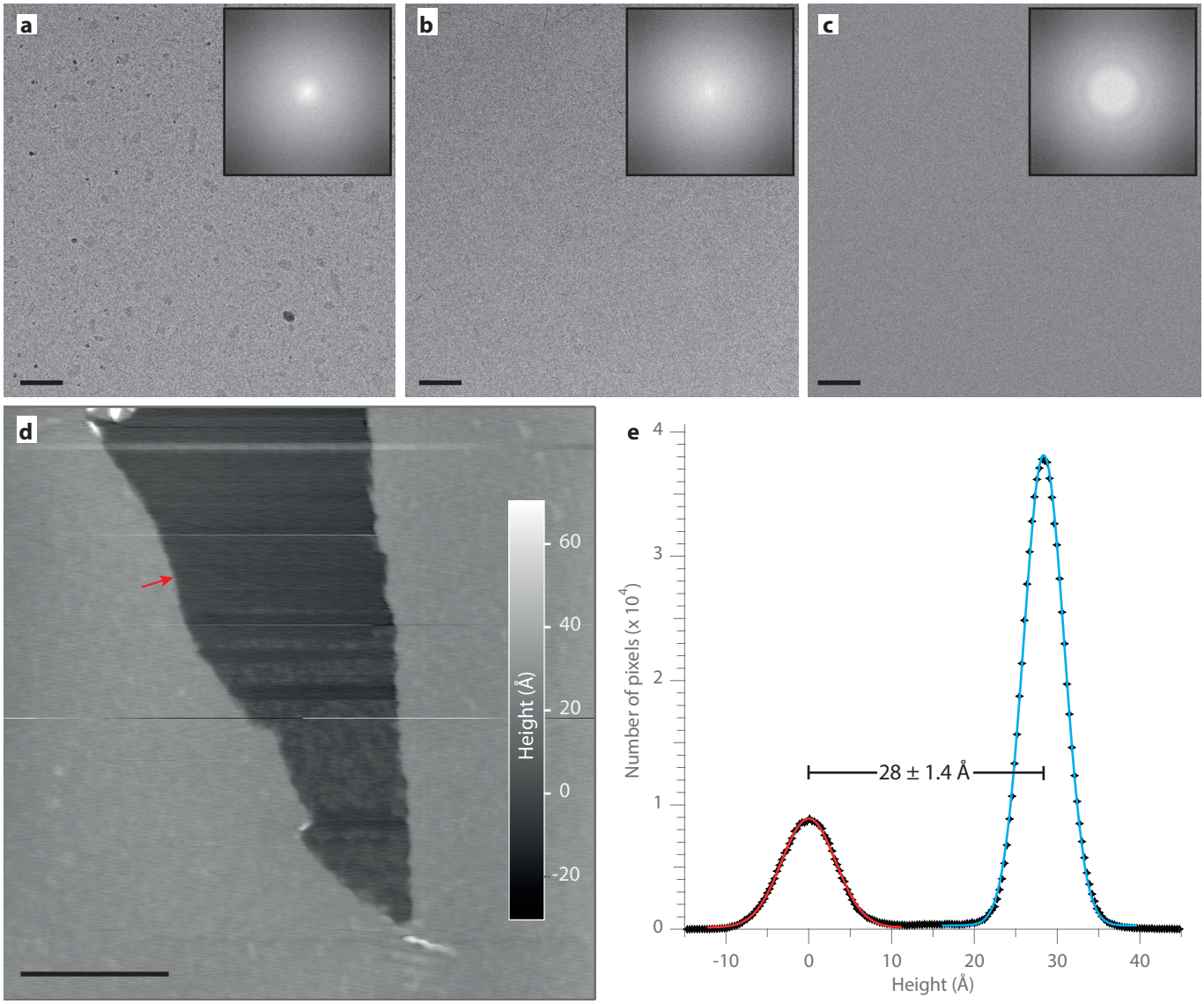

Supplementary Figure 2 | Low-dose images of carbon substrates.
Panel **a** shows untreated graphene, panel **b** is the same sample as **a** after 30 second hydrogen plasma treatment. Panel **c** shows 28 Å thick amorphous carbon for comparison. Insets are the power spectra (FFTs) of each image, reduced to $(1024\ px)^2$, and scale bars are all 2000 Å. Panel **d** is a contact mode atomic force microscopy (AFM) topography image of the edge of the carbon layer from **c** on a mica substrate, which was used to measure the thickness of the carbon layer accurately (scale bar is 5000 Å). Arrow points to the edge of the cleaved carbon layer on the mica substrate. Panel **e** contains a histogram of the height values from **d**, with Gaussian fits to determine the thickness. The smaller red peak is the height of the mica substrate and the larger blue peak is the height on the amorphous carbon layer, and the difference is 28 ± 1.4 Å.

Nature Methods: doi:10.1038/nmeth.2931

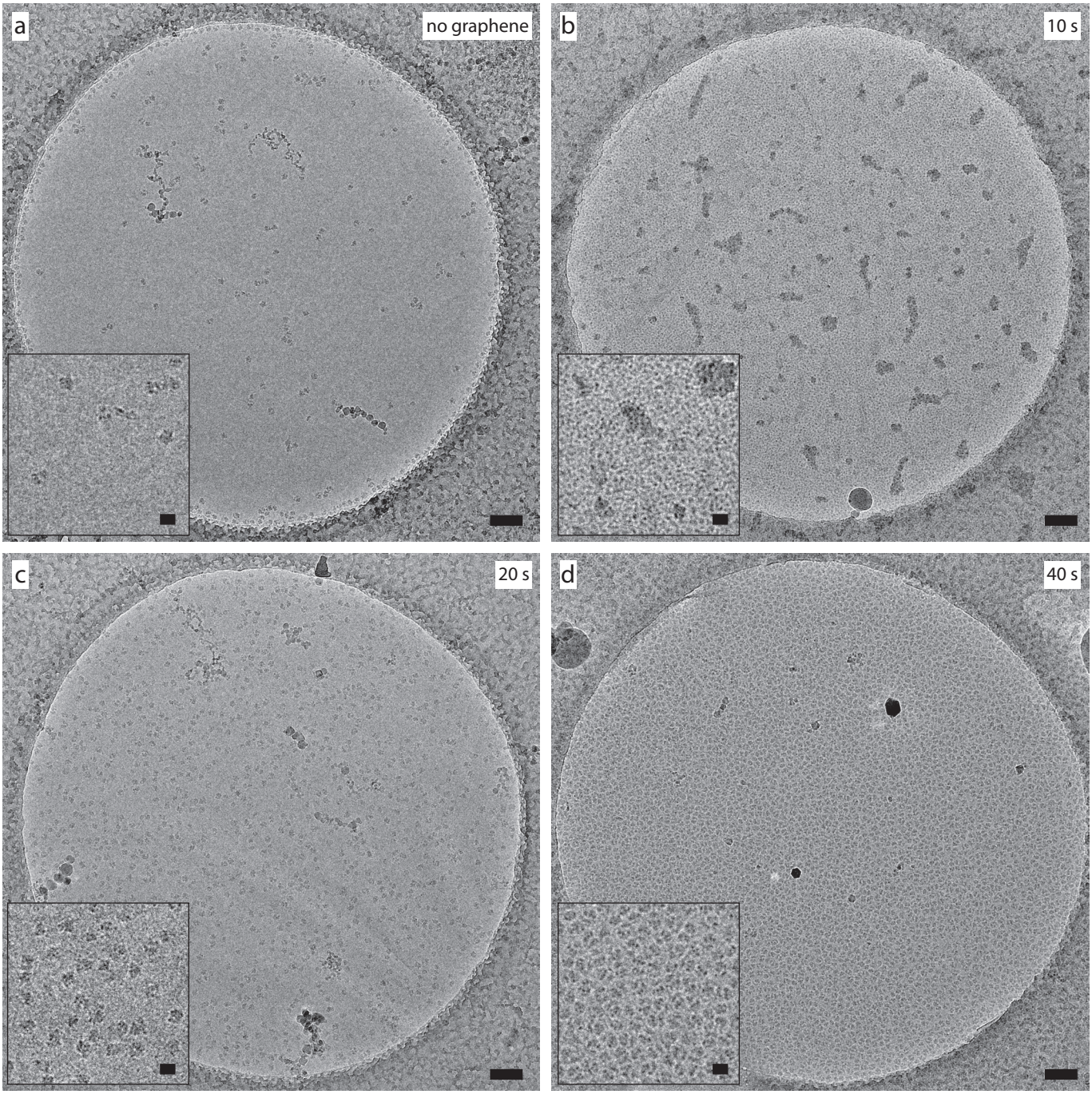

Supplementary Figure 3 | Dose dependent adsorption of ribosomes on hydrogen plasma treated graphene.

Panels **a**-**d** show electron micrographs of 70S ribosomes in vitrified ice at 80 K. Panel **a** is a standard Quantifoil grid treated with a 10 s hydrogen plasma dose. Panels **b**-**d** are Quantifoil grids covered with monolayer graphene, and treated with 10, 20 and 40 s of hydrogen plasma, respectively. All other blotting and vitrification conditions are the same for all four samples. Insets are enlargements of selected regions from each image, showing the typical distribution of particles. Scale bars are 1000 Å for main images and 200 Å for insets.

Nature Methods: doi:10.1038/nmeth.2931

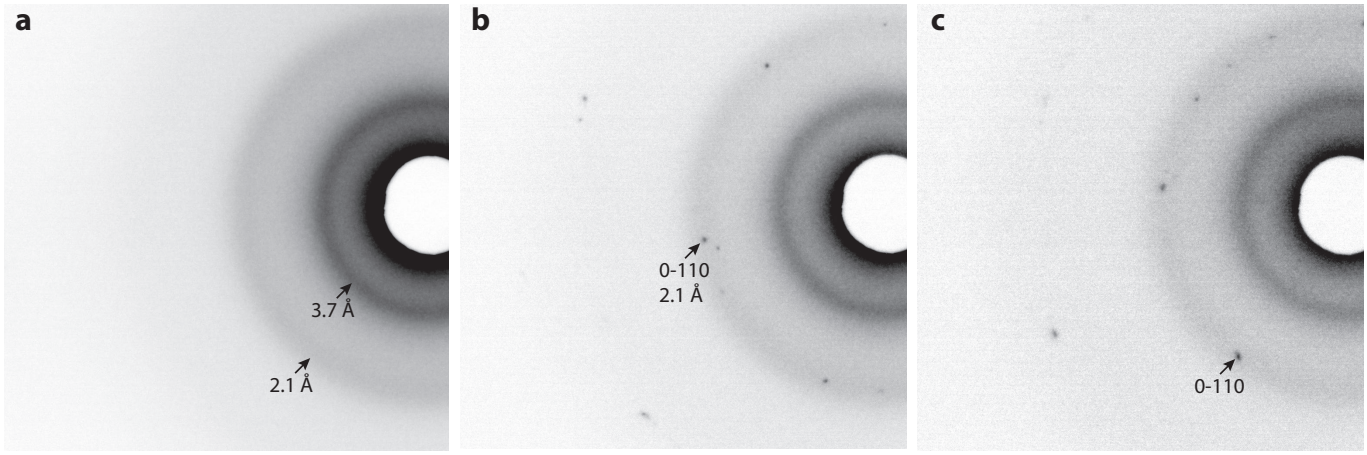

Supplementary Figure 4 | Diffractograms of ribosomes in ice.
Panel **a** shows the selected area diffraction pattern from the unsupported ice in **Fig. 2a**, where the first two diffuse Debye-Scherrer rings for amorphous ice at 3.70 Å and 2.14 Å are indicated with arrows[3]. The white disk at the center is the shadow of the primary beam stop, a homemade platinum ball on a wire. Panel **b** shows the diffraction pattern for the ribosomes in ice on suspended graphene (20 s dose) in **Fig. 2a**, where the 0–110 reflection at 2.14 Å of the monolayer graphene is indicated, and sets the magnification scale for all three diffractograms. Similarly, panel **c** shows the diffractogram for the ribosomes in ice on suspended graphene (40 s dose) for **Fig. 2a**, with the 0–110 peak indicated. Additional diffraction peaks are from small contaminant ice crystals on the surface of the thin film, which are visible in the micrographs. The camera length for each diffractogram is the same, nominally 47 cm.

Nature Methods: doi:10.1038/nmeth.2931

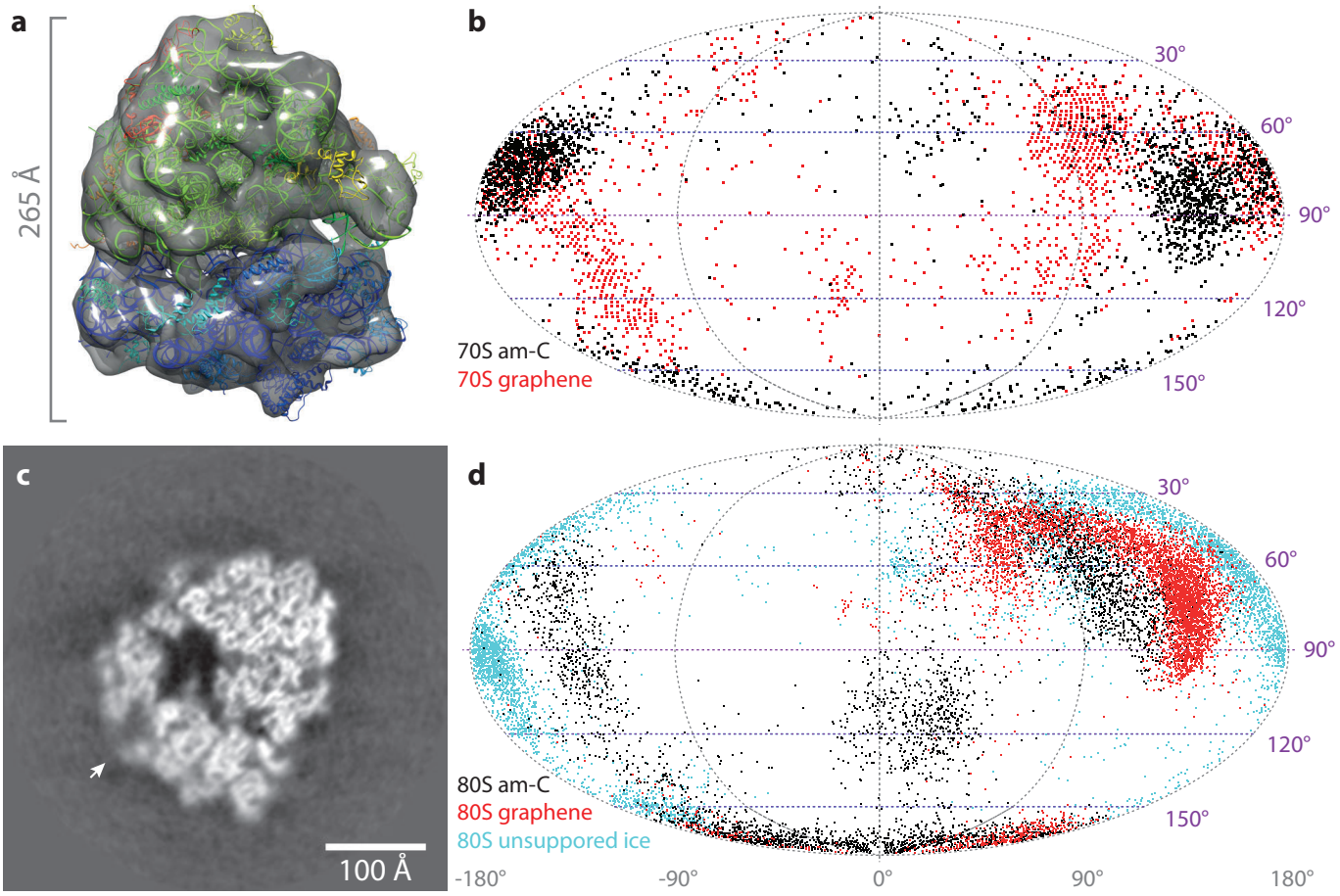

Supplementary Figure 5 | Analysis of ribosome structural data on hydrogen plasma treated graphene. Panel **a** shows a 3D rendering of the density map of the *T. thermophilus* 70S ribosome, reconstructed to 19 Å from three micrographs of particles on graphene. The overlaid ribbon diagram is the rigid-body fit of the crystal structure to the map. Panel **b** is an equal area projection map of the orientation angles of the 2061 ribosomes relative to a graphene substrate (red dots) and an am-C substrate (black dots). Image **c** is a 1.3 Å slice through the unsharpened density map of the *S. cerevisiae* 80S ribosome reconstructed to 5.0 Å on graphene. Blurring of the 40S subunit (arrow) is due to conformational heterogeneity of the sample; this and non-optimal coverage of orientations in Fourier space limit the resolution of the map. Panel **d** is the equal area projection map of the orientations of 10000 80S ribosomes (a randomly selected subset for plotting) from each of three different supports: in ice without a support layer (blue dots), on graphene (red dots) and on am-C (black dots).

Nature Methods: doi:10.1038/nmeth.2931

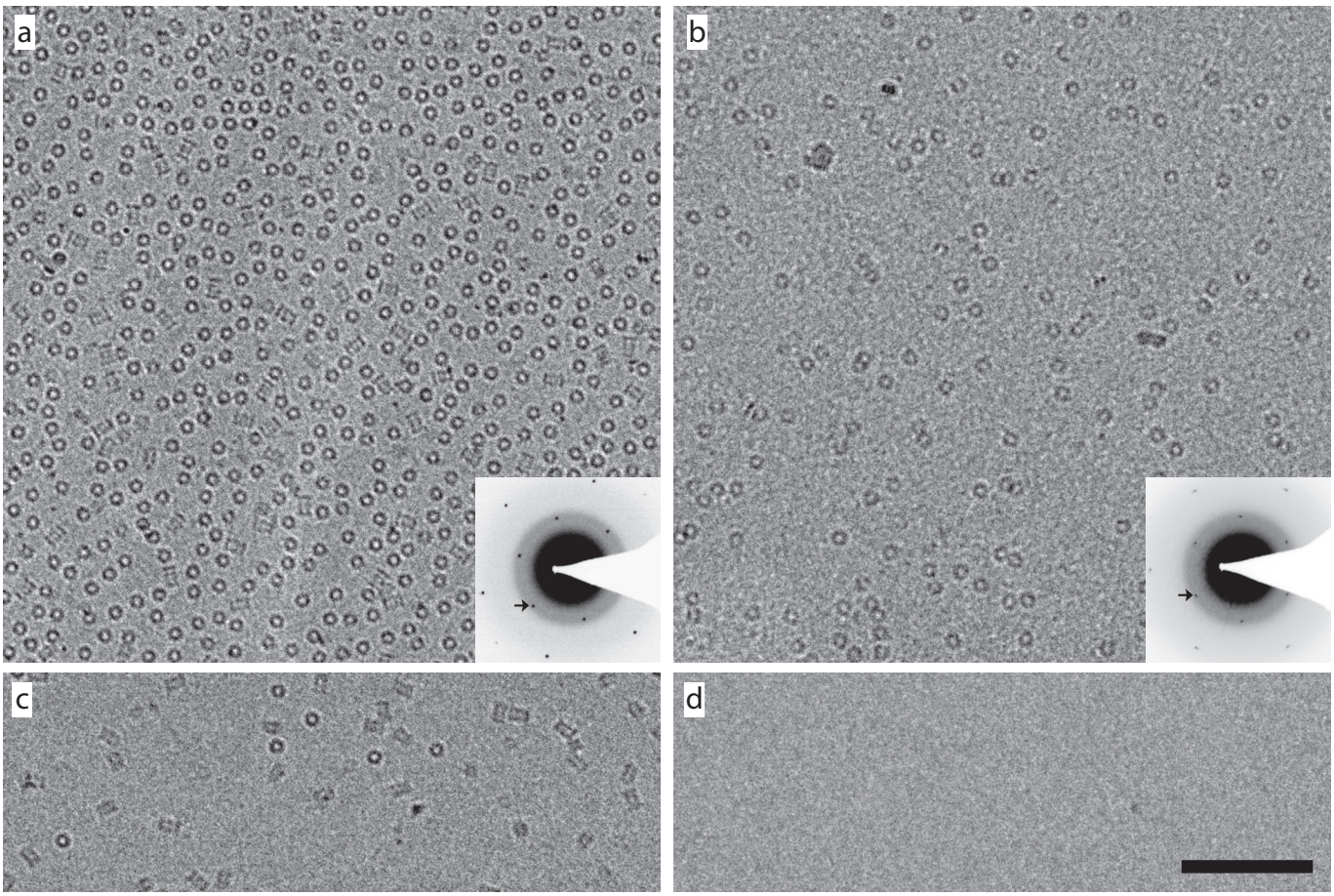

Supplementary Figure 6 | Specific adsorption of proteins to hydrogen plasma treated graphene. Left column comprises electron micrographs of human 20S proteasome in vitreous ice. Panel **a** shows molecules on graphene treated with 40 s of hydrogen plasma and panel **c** shows molecules in ice on an adjacent region of the same grid without graphene. Right column (**b** & **d**) shows the same for horse spleen apoferritin. Insets are the electron diffractograms from the regions imaged, with arrows pointing to the 0-110 graphene reflection. The increase in surface particle density on the graphene support is 6-fold for the proteasome and is likely saturated, and >500-fold for apoferritin. Scale bar is 1000 Å and magnification is the same for all micrographs.

Nature Methods: doi:10.1038/nmeth.2931

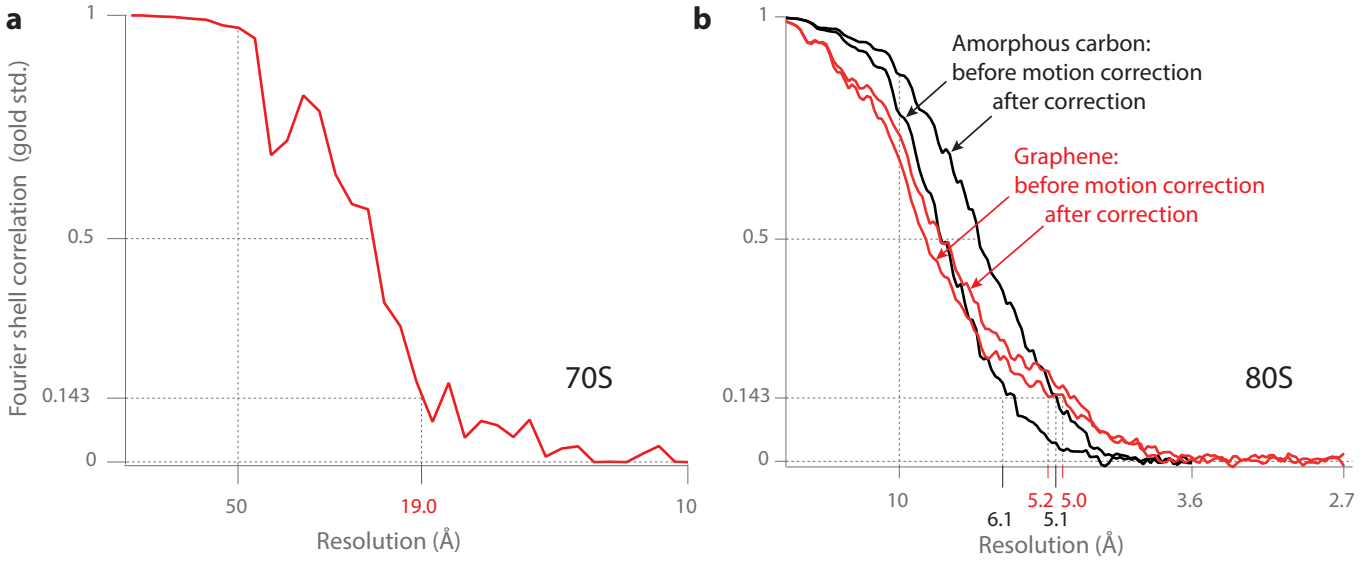

Supplementary Figure 7 | Fourier shell correlation coefficients.
Calculated for the 70S (**a**) and 80S (**b**) ribosomes using the reconstructed electron density map refined from two random halves of the dataset, keeping each separate through the reconstruction process ("gold standard")[30,35]. Using the 0.143 criterion[36], the resolution for the 70S map from 2061 particles on graphene using three micrographs was 19.0 Å. The resolution of the 80S map from 20,050 particles on graphene was 5.2 Å, and showed little improvement to 5.0 Å, with motion correction (**b**, red curves). We compare this to a reconstruction using the same number of particles chosen at random from a previously published dataset on the same ribosome sample where the resolution is 6.1 Å before motion correction and 5.1 Å after motion correction (black curves)[2].

Nature Methods: doi:10.1038/nmeth.2931

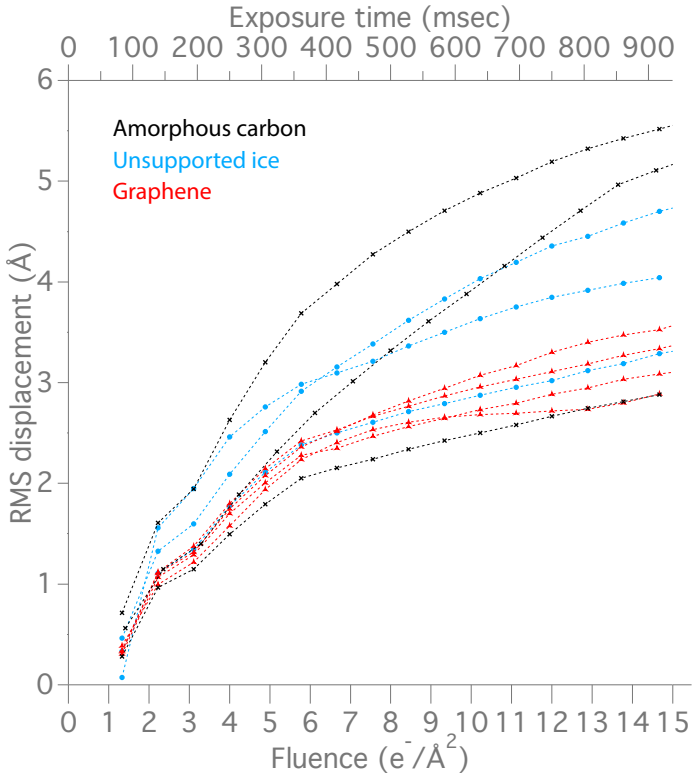

Supplementary Figure 8 | Speed plots of ribosomes on various substrates.
The root mean squared (RMS) displacement from the initial position of 80S ribosomes during electron beam irradiation is measured for ten grids with three different substrates as detailed in the methods: amorphous carbon, unsupported ice and hydrogen plasma treated graphene. Data is the same as contained in **Fig. 3** except plotted together to facilitate comparison. Each curve is calculated from thousands of particles on a single grid. Electron fluence for all experiments was 16 $e^-/Å^2/s$ and energy was 300 keV.

Nature Methods: doi:10.1038/nmeth.2931

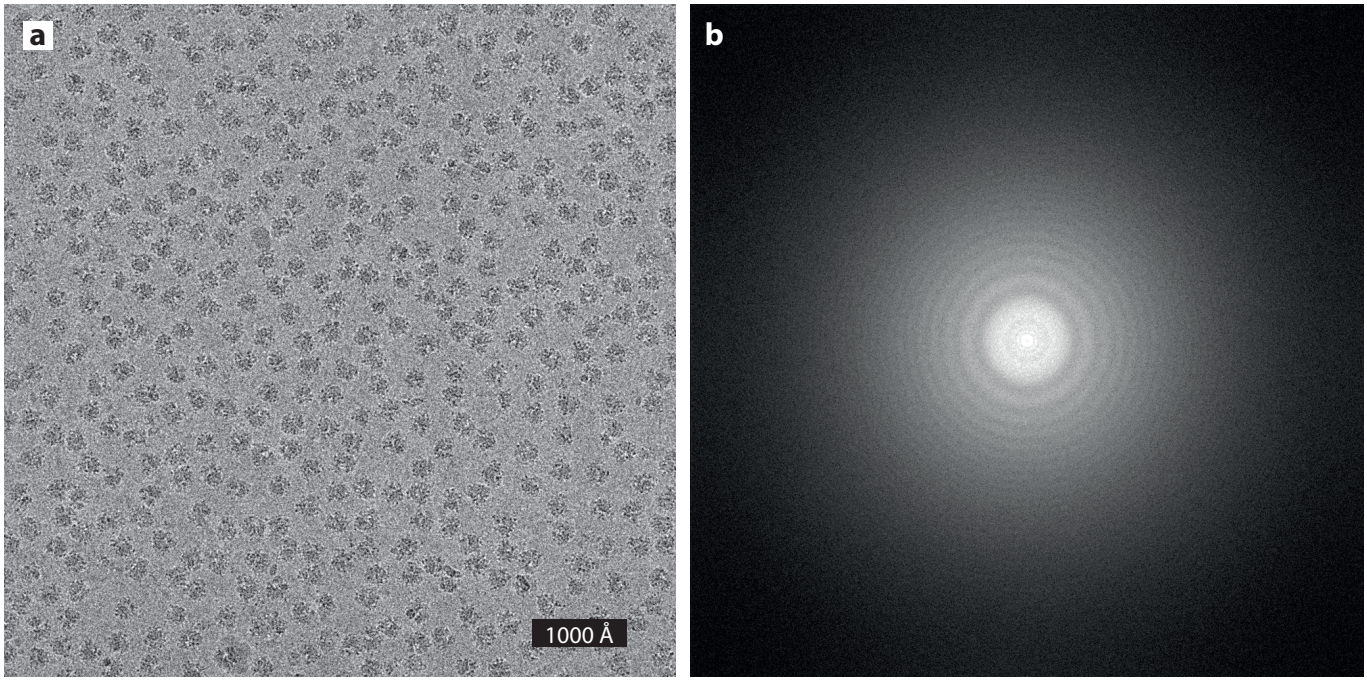

Supplementary Figure 9 | Electron micrograph of 80S ribosomes on graphene.
Panel **a** is a typical micrograph of 80S ribosomes on hydrogen plasma treated graphene. Image was down sampled from 4096 x 4096 pixels (1.7 Å / px) x 16 bits of native resolution to 1024 x 1024 pixels and intensity was scaled to an 8 bit window comprising ± 3σ about the mean intensity value. Panel **b** is the power spectrum of **a**, showing the phase contrast rings from the ribosomes alone, as the graphene does not contribute to spectral frequencies in this range. The focus value for this micrograph was –2.7 μm.

Nature Methods: doi:10.1038/nmeth.2931

Supplementary Table 1 | Radiation-induced particle speed on various substrates (**Fig. 3**).

Substrate	Phase 1		χ^2	Phase 2		χ^2
Unsupported ice	8.0 ± 2.1 Å/s	0.50 ± 0.13 Å/e$^-$/Å^2	0.79	2.2 ± 0.8 Å/s	0.14 ± 0.06 Å/e$^-$/Å^2	0.076
Amorphous carbon	7.5 ± 2.1 Å/s	0.47 ± 0.13 Å/e$^-$/Å^2	0.16	2.8 ± 0.1 Å/s	0.18 ± 0.06 Å/e$^-$/Å^2	0.12
Graphene	6.6 ± 2.1 Å/s	0.41 ± 0.13 Å/e$^-$/Å^2	0.26	1.5 ± 0.8 Å/s	0.092 ± 0.06 Å/e$^-$/Å^2	0.03

Supplementary Note 1 | Calculation of graphene-water interfacial energy.
For a liquid droplet in a gas environment on a solid surface, the liquid-solid interfacial energy, *W*, is related to the equilibrium contact angle between the droplet and the surface, by the Young-Dupré equation:

$$W = \gamma_w(1 + cos\ \theta)$$

where γ_w is the water surface tension, 72 mJ/m (ref. 37). Using the contact angle values from the as-grown graphene sample ($\theta_{gr} = 91 \pm 0.5°$) and the saturation value from the exponential fit to the data, ($\theta_{grh} = 66 \pm 1.3°$) the change in surface energy due to the hydrogen plasma treatment is then just the change in the interfacial energy for the two surfaces:

$$\Delta W = \gamma_w(cos\ \theta_{gr} - cos\ \theta_{grh})$$

which for the values measured is –0.19 ± 0.02 eV/nm^2. While the presence of the copper substrate may cause a small reduction in the measured angle for native graphene[38], it will have negligible effect on the change in angle used to calculate the change in interfacial energy as the substrate will have the same effect on all the measurements.

Supplementary Note 2 | Proposed model of hydrogen-induced changes in graphene-water interfacial energy.
The water-graphene interfacial energy is dominated by hydrophobic interactions between water and the non-polar graphene lattice. Adding hydrogen disrupts the ordering of water molecules near the graphene surface and thus increases the entropy until the separation between hydrogens is comparable to the length scale of water coordination near the surface. Hydrophobic interactions are long-range and decay exponentially with a decay constant of ~1 nm in water[18]. Since (1) the change in interfacial energy we measure saturates with the addition of order one hydrogen / nm^2, and (2) the total change in surface energy is of the same order as the hydrophobic interaction in water, we conclude that the hydrogen plasma treatment primarily makes the graphene lattice hydrophilic by adding hydrogen atoms that disrupt the local ordering of water molecules at the graphene-water interface.

SUPPLEMENTARY REFERENCES

37. Israelachvili, J. N. *Intermolecular and Surface Forces*. (Academic Press, 2011).

38. Shih, C.-J. *et al. Phys. Rev. Lett.* **109,** 176101 (2012).

Nature Methods: doi:10.1038/nmeth.2931